PAPER • **OPEN ACCESS**

Berry phase transition in twisted bilayer graphene

To cite this article: Johannes C Rode *et al* 2016 *2D Mater.* **3** 035005

2D Materials

PAPER

Berry phase transition in twisted bilayer graphene

Johannes C Rode, Dmitri Smirnov, Hennrik Schmidt and Rolf J Haug

Institut für Festkörperphysik, Leibniz Universität Hannover, D-30167 Hannover, Germany

E-mail: rode@nano.uni-hannover.de

Keywords: twisted graphene bilayer, Berry phase, magnetotransport, Fermi velocity

Supplementary material for this article is available online

OPEN ACCESS

RECEIVED
16 March 2016

REVISED
6 June 2016

ACCEPTED FOR PUBLICATION
20 June 2016

PUBLISHED
11 July 2016

Abstract

The electronic dispersion of a graphene bilayer is highly dependent on rotational mismatch between layers and can be further manipulated by electrical gating. This allows for an unprecedented control over electronic properties and opens up the possibility of flexible band structure engineering. Here we present novel magnetotransport data in a twisted bilayer, crossing the energetic border between decoupled monolayers and coupled bilayer. In addition a transition in Berry phase between π and 2π is observed at intermediate magnetic fields. Analysis of Fermi velocities and gate induced charge carrier densities suggests an important role of strong layer asymmetry for the observed phenomena.

Introduction

Stacked multilayer structures of graphene and other two dimensional materials have become subject of rising scientific interest over the last few years [1]. While incorporation of graphene in van der Waals heterostructures leads to exciting new phenomena [2–4], also purely graphene-based structures attracted much attention: rich interlayer coupling phenomena like low-energy van Hove singularities (vHs) and angle-dependent superlattice physics have been predicted and studied experimentally in so called twisted bilayer graphene (TBG) [5–7]. TBG consists of two carbon honeycomb lattices with a certain rotational mismatch of angle θ which qualitatively divides electronic behavior in three angular ranges [7–9]: while exhibiting most complex signatures at the smallest interlayer twist $\theta \lesssim 2°$ [7–10] and effectively pristine monolayer behavior at large $\theta \gtrsim 15°$ [5, 8, 11], the dispersion can be understood via a perturbative model at intermediate angles [5, 6, 11]: in the absence of interlayer coupling the system is described by two rotationally misaligned copies of the monolayer dispersion, which displaces top and bottom layer's Dirac cones by $\Delta K = 2 \cdot \sin\left(\frac{\theta}{2}\right) \cdot K$ in reciprocal space [5, 6] (with $K = \frac{4\pi}{3a}$ and $a = 246$ pm as length of graphene's lattice vector). At an interlayer hopping of magnitude t^{θ}, the individual dispersions merge in vHs at $\pm E_{\mathrm{vHs}} = v_{\mathrm{F}} \cdot \hbar \cdot \frac{\Delta K}{2} - t^{\theta}$ (v_{F} being the Fermi velocity and $\hbar = \frac{h}{2\pi}$ the reduced Planck constant) [6, 8, 11–13]. Thus TBG offers the rare opportunity to study charge carriers around a divergent density of states by standard gating techniques. Additionally the energetic range between vHs features two effectively decoupled systems in closest possible vicinity, associated with phenomena like excitonic condensation, Coulomb drag or quantum capacitive screening of charge [14–19]. To date, TBG have been extensively studied by scanning tunneling microscopy resolving angle dependent moiré superstructures of wavelength

$$\lambda(\theta) = a \Big/ \left(2 \cdot \sin\left(\frac{\theta}{2}\right)\right) \qquad (1)$$

and confirming the predicted vHs in spectroscopy measurements [6, 8, 11–13]. Another powerful tool of investigation lies in magnetotransport experiments which provide access to many of graphene's unique features [20–23]: in magnetic fields applied perpendicular to the sample plane, the Landau level spectrum for TBG is predicted to be divided into two regimes [9, 24–27]: below the vHs, assuming uniform carrier density in the two decoupled layers, Landau levels follow the energetic sequence of a single layer $E_{\mathrm{N}} = \mathrm{sgn}(N) \cdot v_{\mathrm{F}} \sqrt{2e\hbar B\,|N|}$ but appear at doubled filling factors $\nu = \frac{n \cdot h}{B \cdot e} = N \cdot 8$ due to the additional twofold layer degeneracy (e being the elementary charge, B magnetic flux density, N an integer and n the charge carrier density). The Fermi surface in this scenario consists of four cyclotron orbits, enclosing one Dirac point each (K, rotationally displaced K_θ and

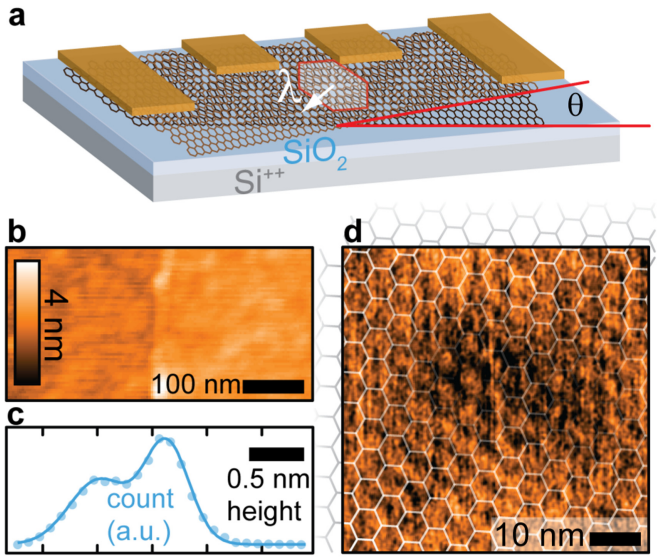

Figure 1. (a) Sketch of a graphene bilayer with angle θ between top and bottom layers´ symmetry directions (red lines) and superlattice of wavelength λ (white arrow). The sample lies on a substrate of doped Si capped with SiO_2 and is contacted in a longitudinal setup. (b) AFM topography of the step between TBG (right) and monolayer graphene (left). (c) Dots: histogram of pixel count over relative height for the topography image in (b). Line: sum of two Gaussian distributions, fit to data. (d) Friction force plot of an AFM scan on the TBG with overlain honeycomb pattern as guide to the eye for the resolved superlattice.

equivalents in opposite valley K' and K'_θ). This corresponds to a topological winding number of $w = \pm 1$ and a Berry phase of $\phi = \pi$ [28]. Above the vHs, different coupling models predict different scenarios: [27] finds a change in carrier polarity within the conduction (valence) band upon crossing the vHs. Cyclotron orbits now enclose a holelike (electronlike) pocket originating from the Γ-point of the superlattice mini Brillouin zone, which leads to secondary Landau fans [9, 27] at a Berry phase of $\phi = 0$. In contrast, [24, 25] find a continuation of the original Landau fan at modified filling factors $\nu = \left(N_+ + \frac{1}{2}\right) \cdot 4$ (with N_+ as nonzero integer) like in a Bernal stacked bilayer [22] ($\theta = 0°$). This scenario works in the extended zone scheme and neglects commensuration effects [24]. Cyclotron orbits around K and K_θ merge into one above the vHs (samefor K' and K'_θ), now enclosing two Dirac points, which corresponds to $w = \pm 2$ and a Berry phase of $\phi = 2\pi$ [28]. The distinguishing experimental factor for one [9, 27] or the other manner of coupling and quantization [24, 25] might be found in the rigorosity and particular formation of the superlattice. Lattice distortions and relaxations undergo qualitative changes towards smaller angles [29] and will further depend on the choice of substrate, which may decide between the superlattice's mini Brillouin zone and the rotated layers´ original Brillouin zones as dominant scale in k-space (see e.g. [7] for the former, leading to backfolding phenomena in small angle TBG). The regime of layer decoupling has been extensively studied in experiment [17–19, 30]: most importantly, electrical gating (top or bottom gate) lifts layer degeneracy, which shows in two superposed sets of monolayerlike Shubnikov-de Haas (SdH) oscillations in longitudinal resistance [17–19, 30]. The coupled regime on the other hand remains quite unexplored in comparison: besides a recent publication [31] on higher energy bands beyond the reach of standard dynamic gating techniques, there has been one report on Bernal-bilayer-like Quantum Hall data in a TBG, which is in line with the second above described model [24, 25]. We here present further evidence for the according scenario, witnessing the corresponding Berry phase transition within a primary Landau fan for the first time.

Experimental results

Sample

Graphene samples are prepared by mechanical exfoliation of natural graphite onto a substrate of SiO_2. Some flakes fold over during this procedure, yielding twisted layers which are processed and contacted for electrical measurements as sketched in figure 1(a). Figure 1(b) shows atomic force microscopy (AFM) topography data over the step between TBG and the uncovered monolayer, revealing a height difference of 6.2 ± 0.2 Å as evident in the histogram in figure 1(c), fit by a double Gaussian distribution. Note that this value is larger than the interlayer spacing in graphite, which is ascribed to the different stacking arrangements [10, 29, 32–34]. Figure 1(d) shows the torsional signal of an AFM scan on the twisted bilayer under investigation, which reveals a periodic structure of 5.7 ± 0.2 nm wavelength fit by an overlain honeycomb pattern. Using equation (1) the corresponding twist angle θ can be calculated as $2.5° \pm 0.1°$.

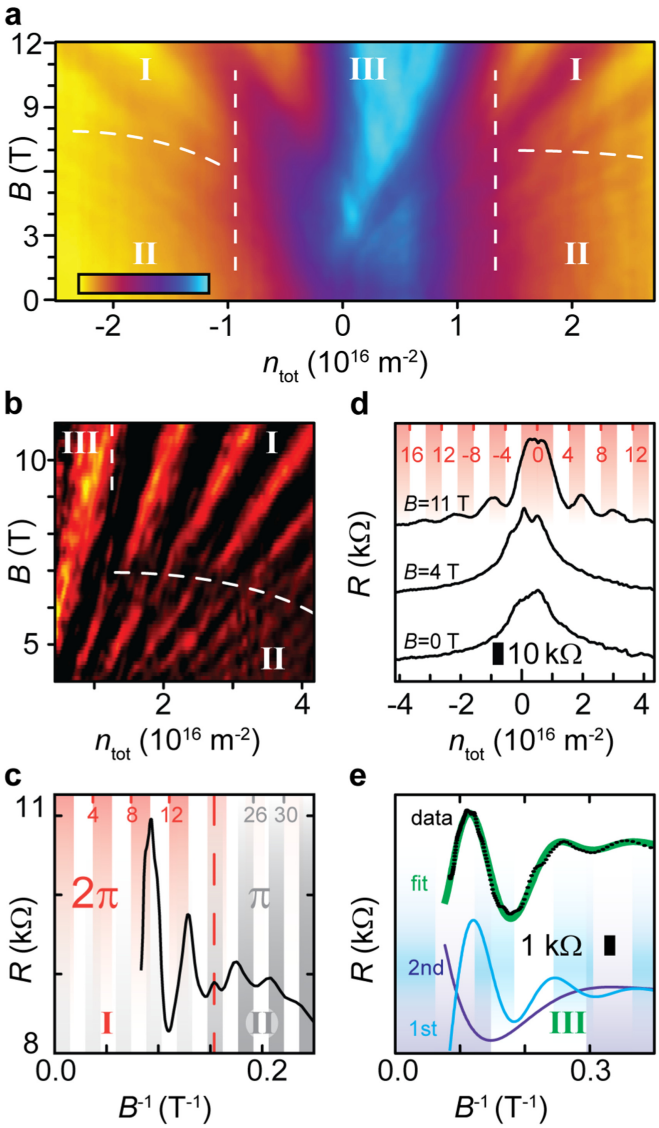

Figure 2. (a) Longitudinal resistance versus total charge carrier density and magnetic field. Dashed lines separate three regions of different magnetotransport behavior. Color scale goes from 6000 to 44 000 Ω (left to right). (b) Differential longitudinal resistance $\frac{dR}{dB}$ versus positive total charge carrier density and magnetic field. Curved horizontal line marks disruption in Landau fan between regions **I** and **II**, dashed vertical line indicates border of region **III**. (c) Resistance versus inverse magnetic field at a fixed total charge carrier density of 2.97×10^{16} m^{-2}. Red dashed line marks transition from $\phi = 2\pi$ to π. Colored tics at top axis indicate filling factors ν, colored bars trace corresponding extrema in oscillations for regimes of 2π (red) and π (gray). (d) Resistance versus total charge carrier density at $B = 11$ T, $B = 4$ T and $B = 0$ T (top to bottom, offset by 30 kΩ). Red tics on top axis indicate filling factors ν at 11 T, red bars trace corresponding extrema in oscillations. (e) Resistance versus inverse magnetic field at a fixed total charge carrier density of 5.4×10^{15} m^{-2}. Top: black dots are data after background removal, green line is the sum of two SdH oscillations with $\phi = \pi$, as fitted to data. Bottom: separately plotted contributions to the fit, colored bars indicate extrema at a monolayer-like sequence of filling factors.

Magnetotransport data

Figure 2(a) shows an overview of longitudinal resistance versus perpendicular magnetic field and the total charge carrier density in both layers n_{tot} induced via the backgate at a temperature of 1.5 K. The data show clear deviations from the commonly expected symmetric Landau fan picture [20–22] and can be divided into three regions, displaying generally different behavior (regions **I** as well as **II** behaving qualitatively analog for both polarities of charge). To demonstrate this more clearly, figure 2(b) shows the derivative $\frac{dR}{dB}$ for positive n_{tot}: while the lowest depicted Landau level at the border of region **III** displays monotonous evolution in the map of B versus n_{tot}, higher Landau levels show an unusual discontinuity around intermediate magnetic fields, separating the data into regions **I** and **II** for $n_{tot} \lesssim 1 \times 10^{16}$ m^{-2}. To quantify this transition, figure 2(c) shows a plot of resistance versus inverse magnetic field at $n_{tot} = 2.97 \times 10^{16}$ m^{-2}. At high magnetic fields ($B^{-1} < 0.15\ T^{-1}$) SdH oscillations are described by a Berry phase of $\phi = 2\pi$ indicating coupled transport [24–26]. For low magnetic fields however ($B^{-1} > 0.15\ T^{-1}$), extrapolation of extrema to a filling

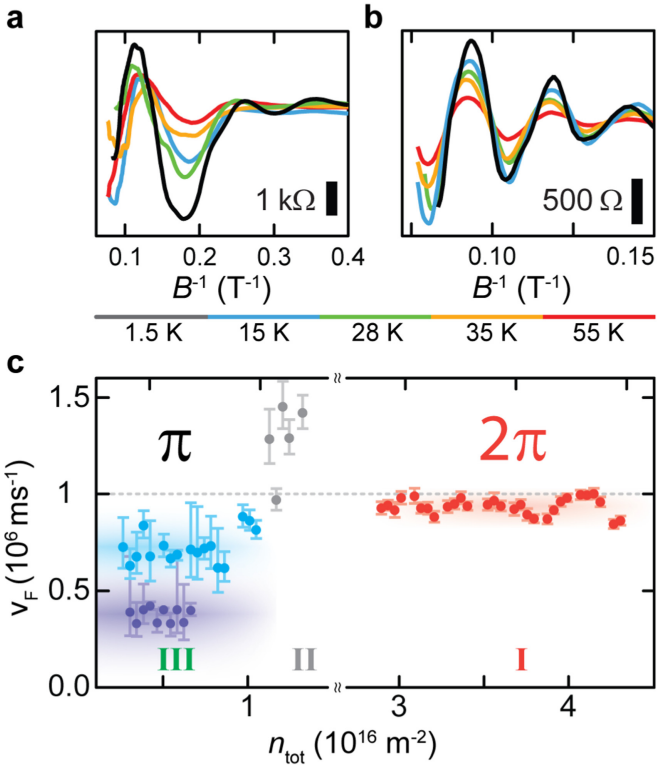

Figure 3. (a) and (b) Resistance versus inverse magnetic field for five different temperatures (color coded according to legend below) at an exemplary total charge carrier density of 5.4 $\times$ 10^{15} m^{-2} (panel a, region **III**) and 3.99 $\times$ 10^{16} m^{-2} (panel b, region **I**). The oscillations have been leveled by removal of a background resistance. (c) Fermi velocities extracted from fits to temperature dependent SdH oscillations as depicted in (a) and (b). Data points within the blue and purple areas in region **III** are extracted from decoupled bottom and top layers´ oscillations respectively. Rising values above $n_{tot} \approx 1 \times 10^{16}$ m^{-2} (gray dots) coincide with the transition to region **II**. Data points within the red colored area stem from the high magnetic field data in region **I**. Error bars originate from fitting uncertainty. The dashed gray line indicates the Fermi velocity of pristine graphene.

factor of $\nu = 0$ reveals a monolayer like quantization of $\phi = \pi$ (see supporting information for more examples and quantitative analysis of the Berry phase).

Figure 2(d) shows cross sections through regions **I** and **III** at $B = 11$ T and through regions **II** and **III** at $B = 4$ and 0 T respectively. The resistance at $B = 11$ T is modulated by pronounced SdH oscillations with $\phi = 2\pi$ confirming the high magnetic field data in figure 2(c). At $B = 4$ T oscillations in region **II** are no longer well pronounced but a double peak around $n_{tot} = 0$ indicates deviation from an ordered zero mode in region **III**. The shoulder around the maximum of the field effect at $B = 0$ T also indicates a more complicated behavior in the low energetic range. To explore this further, figure 2(e) shows resistance versus inverse magnetic flux density at $n_{tot} = 5.4 \times 10^{15}$ m^{-2}: a polynomial background in B has been removed from the data in the top half (black dots, see supporting information for details). The remaining oscillations are fit by the sum of two damped cosine functions (green line) which are plotted separately in the bottom half of the panel (blue, purple lines). As indicated by the colored bars, these superimposed sets of SdH oscillations exhibit a Berry phase of $\phi = \pi$, indicating parallel transport in two decoupled graphene monolayers [17–19, 30].

Fermi velocities

An important theoretical prediction for the low energy dispersion between vHs is a twist angle dependent reduction in Fermi velocity following

$$\frac{v_F^{red}}{v_F^0} = 1 - 9 \cdot \left(\frac{t^\theta}{\hbar \cdot v_F^0 \cdot \Delta K} \right)^2 \qquad (2)$$

with v_F^{red} and v_F^0 as reduced and native Fermi velocity respectively [5, 8, 13]. For $\theta = 2.5°$, equation (2) yields a renormalization factor of 0.62 with the commonly found parameters $v_F^0 = 1 \times 10^6$ ms^{-1} and $t^\theta = 0.1$ eV. Experimentally, Fermi velocities can be extracted from temperature dependence of SdH oscillations [23] as exemplified in figures 3(a) and (b) (see supporting information for examples and details of fitting procedure). Results are depicted in figure 3(c) over a range of positive total charge carrier densities, showing qualitatively different behavior for the three regions introduced in figure 2: low density data points within the blue and purple areas are extracted from the two decoupled layers´ oscillations in region **III**. Both sets of velocities are clearly reduced with respect to pristine graphene. While the bottom layer data (blue, fast oscillations as exemplified in figure 2(e)) center around 0.68×10^6 ms^{-1} close to the expected corresponding reduction value of 0.62, the top layer's velocities (purple) lie even lower at around

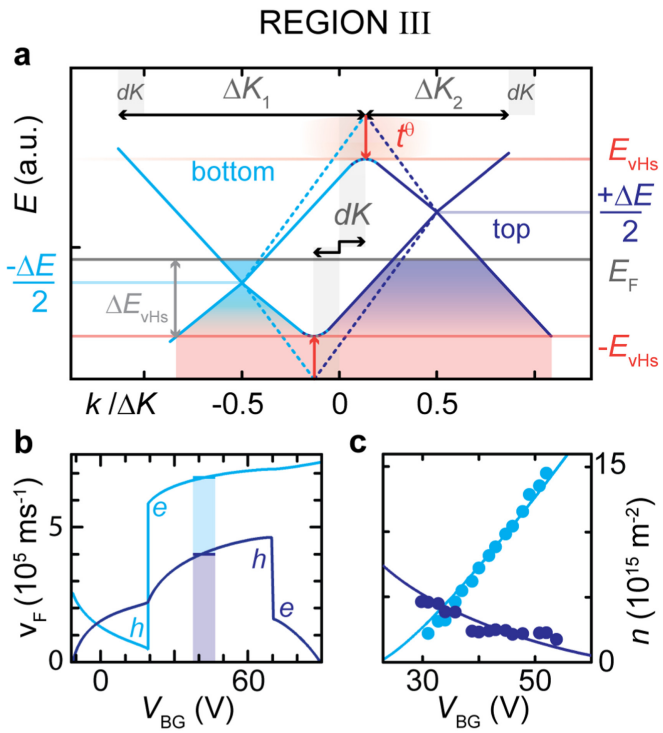

Figure 4. (a) Schematic of low energy dispersion in a gated TBG. Horizontal axis cuts reciprocal plane between bottom (left) and top layer's (right) K-points and is normalized by the magnitude of interlayer displacement vector ΔK. Dashed lines illustrate dispersion in the absence, solid lines under consideration of interlayer coupling t^{θ} (red arrows). The two layers´ Dirac cones intersect at $k/\Delta K = \pm dK$ (gray bars, black arrows) and $E = \pm E_{vHs}$ (red horizontal lines). (b) Renormalized Fermi velocities versus backgate voltage for bottom (blue) and top layer (purple); e and h indicate electron and hole branch respectively. Transparent bars correspond to the average value of measured Fermi velocities in bottom (blue) and top layer (purple). (c) Charge carrier densities versus applied backgate voltage in decoupled bottom (blue) and top (purple) layers. Solid lines illustrate calculations based on screening model in main text, fit to data extracted from frequency of SdH oscillations (dots).

0.4×10^6 ms^{-1}. As we analyze an energetic range of electrons in the bottom and holes in the top layer, we ascribe this discrepancy to electron–hole asymmetry. Like in the present case, stronger reduction in Fermi velocities on the hole side has been found in other TBG [8, 13, 30] and is ascribed to enhanced next-nearest-neighbor hopping [8]. As n_{tot} goes across the border of region **III**, Fermi velocity starts to rise, indicating changes to the dispersion. Because region **II** oscillations are confined to low magnetic fields only however, further velocity data could not be reliably acquired for region **II**. High density data points in the red area stem from high magnetic field oscillations with $\phi = 2\pi$ (region **I**) and center around a constant value of 0.94×10^6 ms^{-1} near the one of native graphene. Note that the lack of a slope in Fermi velocity over energy is indicative of massless carriers and a linear dispersion. This clearly sets our region **I** data apart from a Bernal stacked bilayer and its parabolic dispersion, commonly associated with a Berry phase of 2π.

Decoupled range: layer asymmetry

In the range of effective decoupling (observed in region **III**), a difference Δn_{tb} in the individual layers´ doping charge as well as application of a backgate voltage result in energetic displacement ΔE of the two layers´ Dirac cones [5, 35–37]. This asymmetry in energy leads to a shift in intersection of Dirac cones in k-space by dK as depicted in the schematic in figure 4(a), leading to effective new values $\Delta K_{1,2} = \Delta K \pm 2 \cdot dK$. The renormalizing effect of interlayer coupling t^{θ} on the two layers´ Fermi velocities should therefore be asymmetric and can be estimated by replacing ΔK in equation (2) with $\Delta K_{1,(2)}$ for the positive (negative) half of the bottom layer's Dirac cone and for the negative (positive) half of the top layer's Dirac cone respectively.

This dynamic asymmetry is implemented in the established screening equations [16–19, 36], which may be used to calculate top and bottom layers´ Fermi velocities, charge carrier densities and energetics in dependence on interlayer distance d, twist angle θ, interlayer hopping energy t^{θ} and doping charge in the toplayer δn (see supporting information). Figure 4(b) shows correspondingly calculated Fermi velocities (lines) and measured values (bars) for bottom (blue) and top layer (purple) versus applied backgate voltage V_{BG}. Measured charge carrier densities, extracted from frequency of SdH oscillations in both layers are depicted as dots in figure 4(c), solid lines are calculations based on the screening model. The free parameters of doping charge and interlayer hopping have been adjusted to simultaneously fit both carrier

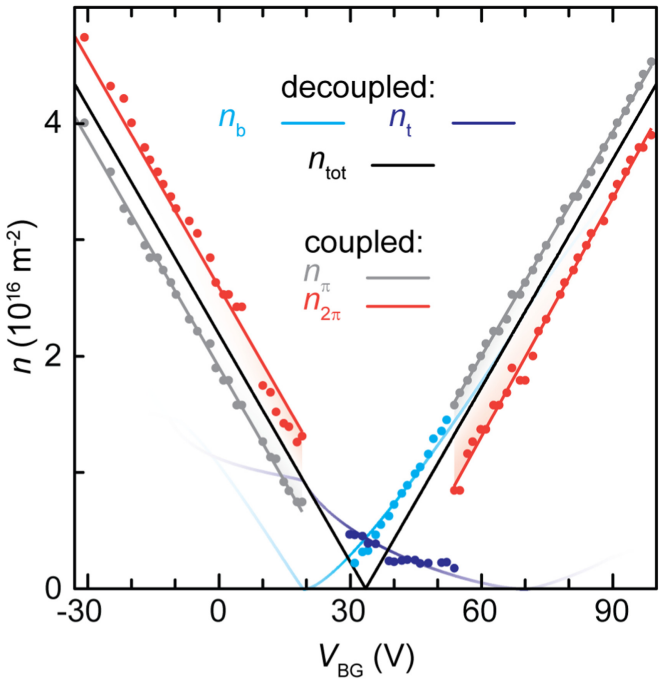

Figure 5. Dots: charge carrier concentrations extracted from frequency of SdH oscillations versus applied backgate voltage in different regimes of quantization (see color coded legend). Blue and purple lines are fit curves based on screening model in main text, black line is correspondingly calculated total charge carrier density. Red and gray lines are linear fits to data collected in the coupled regime.

densities $n_{b,t}$ and measured Fermi velocities $v_F^{b,t}$, yielding values of $\delta n = 1.15 \times 10^{16} \pm 0.10\ \mathrm{m}^{-2}$ and $t_e^\theta = 0.11 \pm 0.01$ eV and $t_h^\theta = 0.15 \pm 0.01$ eV for electrons and holes respectively. The interlayer hopping energy on the electron side t_e^θ is a commonly found value while its counterpart on the hole side t_h^θ lies at the topmost border of reported values [6, 11–13]. The top layer's doping δn may be caused by deposits of processing or environmental chemicals. Extrapolation of the two layers´ densities to $V_{BG} = 0$ V yields similar values i.e. comparable degrees of doping in both layers. Such a symmetric offset in Fermi energy may also be caused by an inherent shift due to breaking of electron–hole symmetry in the TBG [5, 38]. The fits to the decoupled layers´ densities are used to determine a total charge carrier density $n_{tot} = n_b + n_t$, extrapolating the TBG's capacitive coupling to the backgate away from overall charge neutrality.

Coupled range

In addition to the discussed modeling and data for n_b, n_t and n_{tot} in the layer-decoupled region **III**, figure 5 shows charge carrier concentrations extracted at higher energies. Gray dots indicate concentrations extracted from low magnetic field data at $\phi = \pi$ (region **II**), red dots in high magnetic fields at $\phi = 2\pi$ (region **I**). Solid lines are linear fits sharing an absolute slope of $6.59 \pm 0.18 \times 10^{14}\ \mathrm{m}^{-2}\,\mathrm{V}^{-1}$ which is in good agreement with the backgate's calculative capacitive coupling constant $\alpha = 6.53 \times 10^{14}\ \mathrm{m}^{-2}\,\mathrm{V}^{-1}$ and slope of n_{tot} over V_{BG}.

Discussion

This suggests all of the induced charge carriers filling up the examined high-energetic Landau levels, which indicates quantization of a coupled system in the corresponding ranges. Said behavior partly conforms to theory as beyond a certain energy E_{vHs}, layers should merge in a single system [5, 24–26]. The most important prediction for this layer-coupled case is a quantization at Berry phase $\phi = 2\pi$ due to a topologically protected zero mode [24–26]. Furthermore the according charge carriers are expected to retain massless signature up to a critical magnetic flux density which would lie around 45 T for $\theta = 2.5°$ [25]. These criteria are met in region **I** featuring $\phi = 2\pi$ at a constant Fermi velocity. Although these observations comply with theory while regarded on their own, the persistence of Berry phase π at low magnetic fields as well as deviation from n_{tot} in both $n_{2\pi}$ and n_π constitute an interesting deviation from the predicted scenario. We attribute this to strong layer asymmetry in our system, which is not accounted for in the predicted Landau quantization for TBG [24, 25]. In the following we will provide a self-consistent qualitative explanation for the observed deviations from the layer-symmetric case: an important peculiarity lies in the fact, that the transition from region **III** to **II** takes place at a charge carrier concentration n_π close to n_b on the electron side (figure 5 at around $V_{BG} \sim 50$ V) and close to n_t on the hole side (figure 5 at around $V_{BG} \sim 20$ V), while the opposite layer's density is small in comparison. Note that firstly, the transition to n_π at only the dominant layer's density

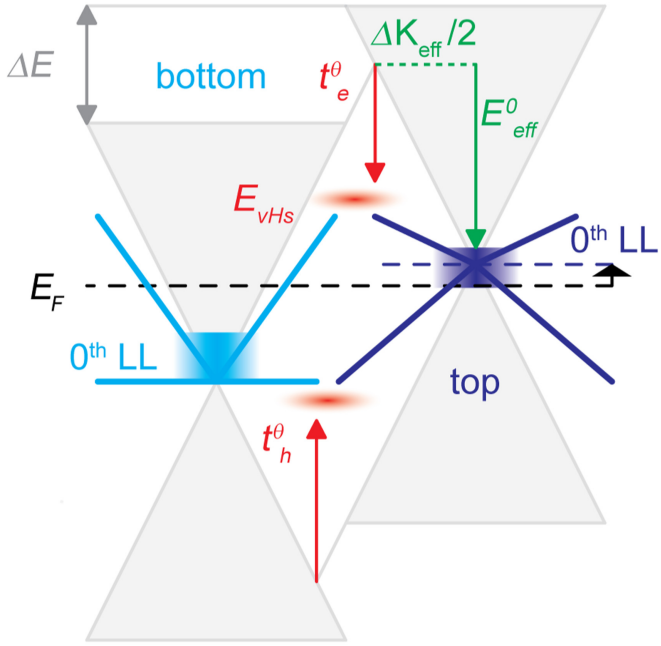

Figure 6. Schematic of the electronic dispersion around the **III-II-I** transition at $V_{BG} = 50$ V ($n_{tot} \approx 1.1 \times 10^{16}$ m^{-2}) and $B = 6.75$ T. Light gray areas are original Dirac cones, displaced by ΔE. Colored lines indicate calculated modifications to the band structure under interlayer hopping energies t^{θ} (red arrows). Green lines indicate momentum $\Delta K_{eff}/2$ and energy E^{0}_{eff} from the top layer's Dirac point to the crossing of cones. Dashed black line marks position of Fermi energy at $B = 0$ T. Purple and blue areas enclose energetic region of charge carriers contracted by the 0th Landau level around the **II-I** transition at $B_{tr} = 6.75$ T. Black arrow and purple horizontal line mark pinning of Fermi energy to the top layer's Dirac point for $B > B_{tr}$.

n_b (or n_t respectively) is consistent with the Berry phase of π in the according oscillations, as a Berry phase of 2π would require the inclusion of both layers´ zero modes [24, 25]. Secondly, exclusion of the other layer's charge may be linked to localization due to strongly reduced Fermi velocities, when interlayer bias renders ΔK_{eff} small (compare $\Delta K_{1,2}$ in figure 4(a)) and the corresponding energy scale E^{0}_{eff} becomes comparable to t^{θ} (see figure 6). Note that the excluded layer's calculated Fermi velocity at the transition point (figure 4(b)) is much smaller than the dominant one's, and even close to zero on the hole side (hole-branch of bottom layer at $V_{BG} \sim 20$ V).

Another interesting cohesion can be found at the **II-I** transition. Figure 6 shows a schematic picture of the calculated dispersion at the triple point between regions **I**, **II** and **III** on the electron side (compare figure 5). The Fermi energy still lies below the vHs and, in the absence of a magnetic field, in the regime of electron conduction for the bottom and hole conduction for the top layer. Around the **II-I** transition at a magnetic field $B_{tr} \approx 6.75$ T (see figure 2) however, the zeroth Landau level of the top layer extends far enough to pin the Fermi energy (purple rectangle, figure 6). Thus, both layer's zero modes may now contribute to the quantization in region **I**, which is in accordance with the observation of Berry phase $\phi = 2\pi$. The vanishing Fermi velocities in the top layer's upper half cone at the transition on the electron side (top layer's electron branch, figure 4) and the nearly flat dispersion in the bottom layer's bottom half cone at the transition on the hole side (bottom layer's hole branch, figure 4) are likely to be connected to the premature onset of coupling just below the calculated vHs. While the above reasoning is short of providing a closed theory on layer-asymmetric TBG, it identifies interesting cohesions in the observed phenomena, encouraging a more detailed theoretical treatment of Landau quantization in tunable TBG systems.

In summary we have studied the magnetotransport behavior in a small angle (2.5°) twisted graphene bilayer produced by folding of a single layer. The measurements show Landau quantization across the transition between a decoupled and coupled TBG system for the first time: at low energies the anticipated layer decoupling is described by a screening model. At higher energies magnetic field divides the coupled range in two regions, quantized at Berry phases of π and 2π respectively. Together with an offset between carrier densities in the different regions we attribute this to strong asymmetry in energy and reduction of Fermi velocities between top and bottom layer.

After submission of this manuscript, very recent experimental indications [39] for the more rigorous backfolding scheme with a change of effective carrier polarity around the vHs [9, 27] came to our notice. A different shaping of the superlattice due to a smaller angle as well as encapsulation of the TBG device is likely to be responsible for the manifestation of the corresponding coupling scenario [9, 27] as opposed to the one evidenced in our present work [24, 25].

Acknowledgments

This work was supported by the DFG within the priority program SPP 1459, graphene and by the School for Contacts in Nanosytems. Johannes C Rode acknowledges support from Hannover School for Nanotechnology. The authors thank Hadar Steinberg for useful discussions.

References

[1] Geim A K and Grigorieva I V 2013 *Nature* **499** 419–25
[2] Ponomarenko L A *et al* 2013 *Nature* **497** 594–7
[3] Dean C R *et al* 2013 *Nature* **497** 598–602
[4] Hunt B *et al* 2013 *Science* **340** 1427–30
[5] Lopes dos Santos J M B, Peres N M R and Castro Neto A H 2007 *Phys. Rev. Lett.* **99** 256802
[6] Li G, Luican A, Lopes dos Santos J M B, Castro Neto A H, Reina A, Kong J and Andrei E Y 2010 *Nat. Phys.* **6** 109–13
[7] Schmidt H, Rode J C, Smirnov D and Haug R J 2014 *Nat. Commun.* **5** 5742
[8] Luican A, Li G, Reina A, Kong J, Nair R R, Novoselov K S, Geim A K and Andrei E Y 2011 *Phys. Rev. Lett.* **106** 126802
[9] Wang Z F, Liu F and Chou M Y 2012 *Nano Lett.* **12** 3833–8
[10] Uchida K, Furuya S, Iwata J-I and Oshiyama A 2014 *Phys. Rev.* B **90** 155451
[11] Brihuega I, Mallet P, González-Herrero H, Trambly de Laissardière G, Ugeda M M, Magaud L, Gómez-Rodríguez J M, Ynduráin F and Veuillen J-Y 2012 *Phys. Rev. Lett.* **109** 196802
[12] Yan W, Liu M, Dou R-F, Meng L, Feng L, Chu Z-D, Zhang Y, Liu Z, Nie J-C and He L 2012 *Phys. Rev. Lett.* **109** 126801
[13] Yin L-J, Qiao J-B, Wang W-X, Zuo W-J, Yan W, Xu R, Dou R-F, Nie J-C and He L 2015 *Phys. Rev.* B **92** 201408
[14] Min H, Bistritzer R, Su J-J and MacDonald A H 2008 *Phys. Rev.* B **78** 121401
[15] Perali A, Neilson D and Hamilton A R 2013 *Phys. Rev. Lett.* **110** 146803
[16] S Kim S and Tutuc E 2012 *Solid State Commun.* **152** 1283–8
[17] Schmidt H, Lüdtke T, Barthold P, McCann E, Fal'ko V I and Haug R J 2008 *Appl. Phys. Lett.* **93** 172108
[18] Sanchez-Yamagishi J D, Taychatanapat T, Watanabe K, Taniguchi T, Yacoby A and Jarillo-Herrero P 2012 *Phys. Rev. Lett.* **108** 076601
[19] Fallahazad B, Hao Y, Lee K, Kim S, Ruoff R S and Tutuc E 2012 *Phys. Rev.* B **85** 201408
[20] Novoselov K S, Geim A K, Morozov S V, Jiang D, Katsnelson M I, Grigorieva I V, Dubonos S V and Firsov A A 2005 *Nature* **438** 197–200
[21] Zhang Y, Tan Y-W, Stormer H L and Kim P 2005 *Nature* **438** 201–4
[22] Novoselov K S, McCann E, Morozov1 S V, Fal'ko V I, Katsnelson M I, Zeitler U, Jiang D, Schedin F and Geim A K 2006 *Nat. Phys.* **2** 177–80
[23] Zou K, Hong X and Zhu J 2011 *Phys. Rev.* B **84** 085408
[24] de Gail R, Goerbig M O, Guinea F, Montambaux G and Castro Neto A H 2011 *Phys. Rev.* B **84** 045436
[25] Choi M-Y, Hyun Y H and Kim Y 2011 *Phys. Rev.* B **84** 195437
[26] Lee D S, Riedl C, Beringer T, Castro Neto A H, von Klitzing K, Starke U and Smet J H 2011 *Phys. Rev. Lett.* **107** 216602
[27] Moon P and Koshino M 2012 *Phys. Rev.* B **85** 195458
[28] de Gail R, Goerbig M O and Montambaux G 2012 *Phys. Rev.* B **86** 045407
[29] van Wijk M M, Schuring A, Katsnelson M I and Fasolino A 2015 *2D Mater.* **2** 034010
[30] Schmidt H, Lüdtke T, Barthold P and Haug R J 2010 *Phys. Rev.* B **81** 121403
[31] Hong S J *et al* 2016 *Synth. Met.* **216** 65–71
[32] Berashevich J and Chakraborty T 2011 *Phys. Rev.* B **84** 033403
[33] Shibuta Y and Elliott J A 2011 *Chem. Phys. Lett.* **512** 146–50
[34] Jung J, DaSilva A M, MacDonald A H and Adam S 2015 *Nat. Commun.* **6** 6308
[35] Xian L, Barraza-Lopez S and Chou M Y 2011 *Phys. Rev.* B **84** 075425
[36] Chung T-F, He R, Wu T-L and Chen Y P 2015 *Nano Lett.* **15** 1203–10
[37] Huang S, Yankowitz M, Chattrakun K, Sandhu A and LeRoy B J 2015 arXiv:1504.08357 [cond-mat.mtrl-sci]
[38] Charlier J-C, Michenaud J-P and Lambin P 1992 *Phys. Rev.* B **46** 4540
[39] Kim Y, Herlinger P, Moon P, Koshino M, Taniguchi T, Watanabe K and Smet J H 2016 arXiv:1605.05475[cond-mat.mes-hall]